Hindawi
Concepts in Magnetic Resonance Part A
Volume 2019, Article ID 5895206, 11 pages
https://doi.org/10.1155/2019/5895206

Research Article

Magic Angle Spinning and Truncated Field Concept in NMR

J. Jenczyk

NanoBioMedical Centre, Adam Mickiewicz University, Wszechnicy Piastowskiej 3, 61-614 Poznań, Poland

Correspondence should be addressed to J. Jenczyk; jacjen@amu.edu.pl

Received 7 May 2019; Revised 1 July 2019; Accepted 5 September 2019; Published 4 December 2019

Academic Editor: Giacomo Parigi

In order to thoroughly comprehend and adequtely interpret NMR data, it is necessary to perceive the complex structure of spin Hamiltonian. Although NMR principles have been extensively discussed in a number of distinguished introductory publications, it still remains difficult to find illustrative graphical models revealing the tensorial nature of spin interaction. Exposure of the structure standing behind mathematical formulas can clarify intangible concepts and provide a coherent image of basic phenomena. This approach is essential when it comes to hard to manage, time-dependent processes such as Magic Angle Spinning (MAS), where the anisotropic character of the spin system interactions couple with experimentally introduced time evolution processes. The presented work concerns fundamental aspects of solid state NMR namely: the uniqueness of the tetrahedral angle and evolution of both dipolar D and chemical shield σ coupling tensors under MAS conditions.

1. Introduction

Developed conceptually in the 1950s [1, 2] Magic Angle Spinning (MAS) has become a routine technique in solid state NMR spectroscopy [3]. This unique concept, together with the exceptional progress made in the field of NMR probe engineering, has made possible the acquisition of high resolution spectra for rigid phase samples. Commonly used, modern probes now allow for spinning the sample under magic angle conditions, reaching rotation frequencies up to dozens of kilohertz [4]. MAS eliminates the broadening of NMR signals by orientation-dependent spin interactions, yielding significant improvements in resolution and signal-to-noise ratio. The excellent resolution observed in the case of liquid samples stems from the fact that during NMR signal acquisition each molecule undergoes extremely fast and random tumbling. Accordingly, both dipolar and quadrupolar interactions are effectively averaged out and only an isotropic chemical shielding is manifested in the spectrum, together with a subtle J coupling effect. In contrast, solid state spectra usually exhibit peaks which are substantially broadened by dipolar coupling and chemical shift anisotropy (and quadrupolar coupling in the case of quadrupolar nuclei). NMR spectra of powdered solids are thus difficult to analyze due to signal overlap. It can be assumed that the nuclear positions within a crystal lattice are roughly time independent and therefore the crystal orientation, with respect to the external magnetic field, defines the effective Larmor frequency for each individual nucleus within the lattice. For single crystal measurements the manipulation of the sample holder orientation itself can lead to a change of the NMR peak positions [5, 6]. On the contrary, powdered samples, consisting of a large ensemble of randomly oriented tiny crystals, reveal broad NMR spectra representing superposition of lines at all possible frequencies (orientations) weighed by their probability. Both the abovementioned results are due to the anisotropic nature of spin interactions. The work presented below (i) introduces the concept of truncated field which represents the effective local magnetic field generated by dipolar nucleus ($I = 1/2$) under the influence of Zeeman field, (ii) illustrates the tensorial character of dipolar coupling and chemical shift anisotropy (CSA), and (iii) explains the influence of MAS on spin systems.

2. Discussion

2.1. Dipolar Interactions–Truncated Field Concept. According to classic electromagnetism an isolated and noninteracting nucleus with nonzero spin should produce local magnetic field having toroidal geometry (magnetic field lines representation in 3D) as presented in Figure 1(b). An analog geometry of field surfaces can be observed for an ideal and superconductive coil depicted in Figure 1(a). It is known that in this particular case the magnetic moment μ_c depends on current, number of coil turns N, and the coil diameter.

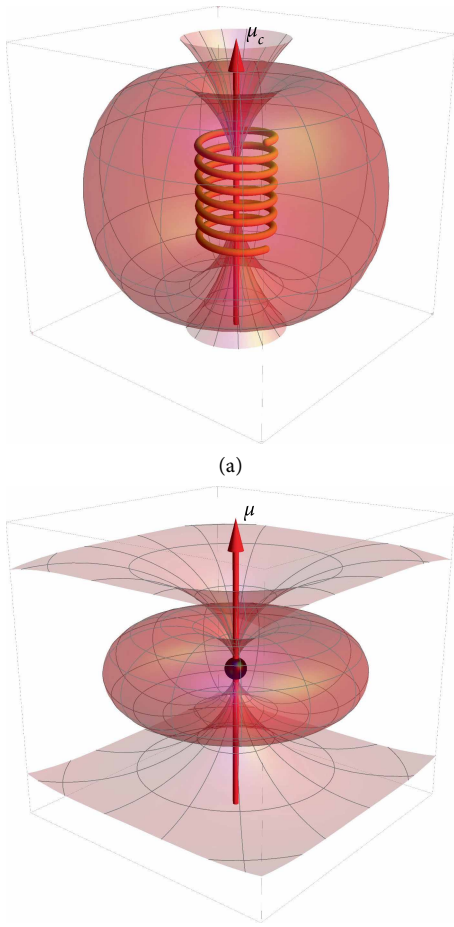

FIGURE 1: (a) Magnetic field geometry produced by a coil, (b) local magnetic field produced by an isolated nucleus having nonzero spin.

Each nucleus with nonzero spin, placed within external magnetic field B_0 obeys the space quantization of angular momentum and its quantum state can be described using discrete Zeeman eigenstates. A nuclear magnetic moment interacting with B_0 experiences torque and, accordingly, Larmor precession takes place. It appears that the quantum state $|\psi\rangle$ of the $(I = 1/2)$ nucleus can be represented as a linear combination of only two so-called basis states $|\uparrow\rangle$ and $|\downarrow\rangle$ weighted by complex number coefficients $c_\uparrow$ and $c_\downarrow$. Spatial quantization rules imply that in the pure state, spin precess over a double cone surface with a specified apex angle exactly equals the tetrahedral angle (details presented in Supplementary 1). In order to formally describe this mechanism it is possible to analyze one arbitrarily chosen surface S (Equation 1 – discussed in Supplementary 1) of local magnetic field and subsequently subject it to rotation transformations.

$$S = \begin{pmatrix} \cos(\varphi)[a - a\cos(\theta)] \\ \sin(\varphi)[a - a\cos(\theta)] \\ \sin(\theta) \end{pmatrix}. \quad (1)$$

where φ and θ are azimuthal and polar angles, respectively in spherical coordinate system representation. According to spatial quantization rule it is necessary to tilt the surface S following the inclination of nuclear magnetic moment vector in B_0.

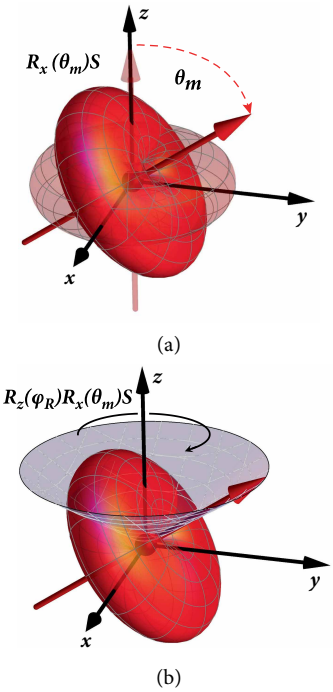

FIGURE 2: (a) $R_x(\theta_m)S$ and (b) $R_z(\varphi_R)R_x(\theta_m)S$ operations.

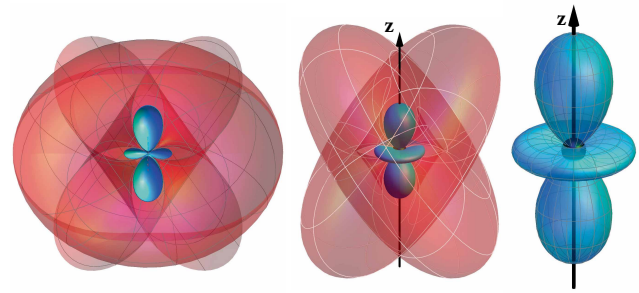

FIGURE 3: The truncated field represents phase independent, constant magnetic field space which can be described by Laplace's spherical harmonic $Y_2^0(\varphi, \theta)$.

This can be done using rotation matrix $R_x(\theta)$ with specifically chosen magic angle $\theta_m \approx 54.74^\circ$(half of the tetrahedral angle). The operation is presented in Figure 2(a) and described mathematically below.

$$R_x(\theta_m)S = \begin{pmatrix} 1 & 0 & 0 \\ 0 & \cos(\theta_m) & -\sin(\theta_m) \\ 0 & \sin(\theta_m) & \cos(\theta_m) \end{pmatrix} \begin{pmatrix} \cos(\varphi)[a - a\cos(\theta)] \\ \sin(\varphi)[a - a\cos(\theta)] \\ \sin(\theta) \end{pmatrix}, \quad (2)$$

$$R_x(\theta_m)S = \begin{pmatrix} \cos(\varphi)[a - a\cos(\theta)] \\ \cos(\theta_m)\sin(\varphi)[a - a\cos(\theta)] - \sin(\theta_m)\sin(\theta) \\ \sin(\theta_m)\sin(\varphi)[a - a\cos(\theta)] + \cos(\theta_m)\sin(\theta) \end{pmatrix}. \quad (3)$$

Subsequently, it is necessary to introduce spin precession which is equivalent to the local potential $R_x(\theta_m)S$rotation around z-axis. In order to do so it is possible to operate another rotation matrix $R_z(\varphi_R)$ as described below and presented in Figure 2(b).

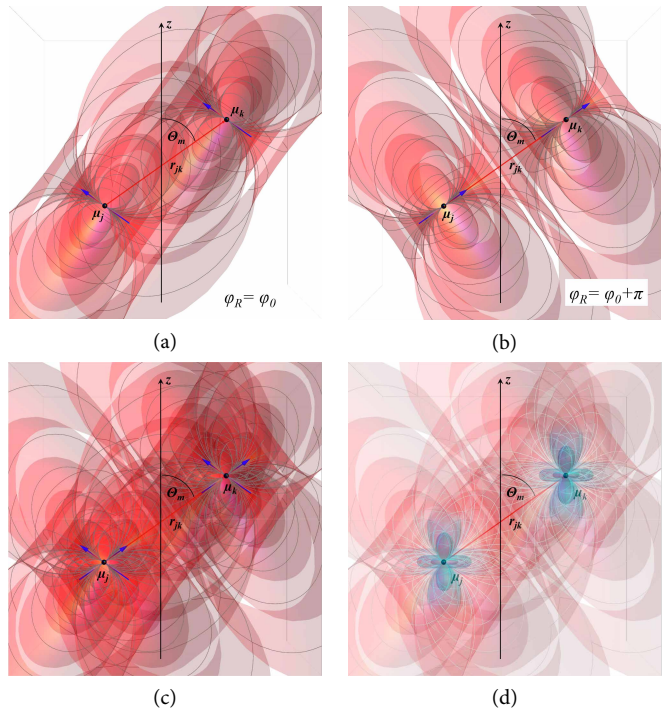

FIGURE 4: Pair of spins (having the same phase) distanced by vector r_{jk} presented for two different phases (a) $\varphi_R = \varphi_0$ and (b) $\varphi_R = \varphi_0 + \pi$, respectively. (c) Represents merging of two phases, and (d) illustrates truncated field symmetries for both spins residing in high external magnetic field B_o.

$$R_z(\varphi_R)R_x(\theta_m)S = \begin{pmatrix} \cos(\varphi_R) & -\sin(\varphi_R) & 0 \\ \sin(\varphi_R) & \cos(\varphi_R) & 0 \\ 0 & 0 & 1 \end{pmatrix} \begin{pmatrix} \cos(\varphi)[a - a\cos(\theta)] \\ \cos(\theta_m)\sin(\varphi)[a - a\cos(\theta)] - \sin(\theta_m)\sin(\theta) \\ \sin(\theta_m)\sin(\varphi)[a - a\cos(\theta)] + \cos(\theta_m)\sin(\theta) \end{pmatrix}. \tag{4}$$

$$R_z(\varphi_R)R_x(\theta_m)S = \begin{pmatrix} \cos(\omega_0 t)\cos(\varphi)[a - a\cos(\theta)] - \sin(\omega_0 t)\{\cos(\theta_m)\sin(\varphi)[a - a\cos(\theta)] - \sin(\theta_m)\sin(\theta)\} \\ \sin(\omega_0 t)\cos(\varphi)[a - a\cos(\theta)] + \cos(\omega_0 t)\{\cos(\theta_m)\sin(\varphi)[a - a\cos(\theta)] - \sin(\theta_m)\sin(\theta)\} \\ \sin(\theta_m)\sin(\varphi)[a - a\cos(\theta)] + \cos(\theta_m)\sin(\theta) \end{pmatrix}. \tag{5}$$

where $\varphi_R = \omega_0 t$ is precession angle which can be also called a spin phase, and ω_0 is Larmor angular frequency. It is worth looking closely at the effective local potential when several different phases are merged together as illustrated in Figure 3. There is something very intriguing about local field precession, namely there is a phase independent, constant magnetic field space resembling the symmetry of 3d spin orbital [7–9]. In the high external magnetic field approximation conditions, this effective, local nuclear magnetic field can be described by the second degree, zero order Laplace's spherical harmonic $Y_2^0(\varphi, \theta)$ and it is called truncated field. Knowing the geometry of the truncated field it is subsequently relatively easy to explain an angular dependence of internuclear interactions and elucidate the idea of MAS technique.

Describing a certain type of spin interactions it is possible to use a general tensorial formula (6) linking the spin I_j and the source of the local field B_{loc} experienced by the spin, taking into consideration an orientational dependence of interaction via a second-rank coupling tensor. In the case of dipolar coupling the source of B_{loc} would be the neighbouring spin I_k and the coupling tensor D has the following form [10] (detailed discussion presented in Supplementary 1),

$$\mathcal{H}_{dd} = h d_{jk} \left(I_j \, D \, I_k \right). \tag{6}$$

$$D = \begin{bmatrix} \left(r_{jk}^2 - 3x^2\right)/r_{jk}^2 & -3xy/r_{jk}^2 & -3xz/r_{jk}^2 \\ -3xy/r_{jk}^2 & \left(r_{jk}^2 - 3y^2\right)/r_{jk}^2 & -3yz/r_{jk}^2 \\ -3xz/r_{jk}^2 & -3yz/r_{jk}^2 & \left(r_{jk}^2 - 3z^2\right)/r_{jk}^2 \end{bmatrix}, \tag{7}$$

where h is the Planck constant, and d_{jk} is the direct dipolar coupling constant which is inversely proportional to the r_{jk}^3 (internuclear vector) and depends on the type of interacting nuclei. It is worth looking closely at the structure of the above mentioned matrix and characterizing its main properties in detail. It is clear that the principal axis of D is aligned along z direction when r_{jk} is parallel to z and that the D tensor is symmetrical $\left(D_{\alpha\beta} = D_{\beta\alpha}\right)$. The matrix determinant equals zero when r_{jk} is tilted at the magic angle $(\theta \approx 54.73^\circ)$ with respect to the principal axis (when x,y,z- components are equal). This implies that, no matter how close the two adjacent spins I_j and I_k are, they do not "sense" one another as long as the magic angle alignment of r_{jk} is fulfilled.

This nonintuitive conclusion may be explained relying on the truncated field symmetry in a following way; imagine that

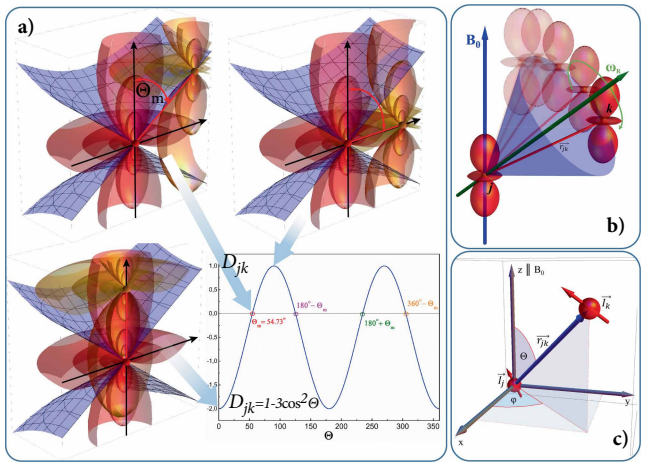

FIGURE 5: (a) Graphical representation of angular dependence of dipolar coupling strength described by the 2nd Legendre polynomial. Coloured in red and in orange are effective local magnetic fields produced by I_j and I_k spins respectively, (b) certain arbitrarily chosen pair of spins under magic angle spinning conditions, and (c) frame of reference for two interacting spins.

there are two nuclear magnetic moments μ_j and μ_k distanced one from another by vector r_{jk} which is oriented under magic angle with respect to the z axis. We can assume that both spins are on the lower energy state ("parallel" to theB_o) and they have the same phase. Of course in general both spins can have completely different and random phases. (this is done for the sake of presentation only). Furthermore, let us assume that μ vectors precess over the cone with specified tetrahedral apex angle. Accordingly, we can define local magnetic field structure at certain specific and arbitrarily chosen moment. Figures 4(a) and 4(b) present two different stages differing in phase by 180 degree. In the case of high external magnetic field approximation, it is possible to define certain effective local magnetic fields, averaging the structure over all possible phases. In order to estimate the symmetry of these truncated magnetic fields two Figure 4(a) and 4(b) were merged giving the pattern illustrated in Figure 4(c). Eventually, well known 3d orbital symmetry pattern emerges which is shown in Figure 4(d).

As shown in Figure 5(a), the strongest interaction between a pair of spins occurs when the internuclear vector r_{jk} is parallel to the external magnetic field B_0. It is also evident that when both spins lay onto the precession cone surface, the dipolar coupling vanishes. It is also worth pointing out that MAS does not affect the orientation of the local effective nuclear magnetic field with respect to B_0. This is illustrated in Figure 5(b). Let us imagine that spin I_j is positioned exactly at the rotor's main axis (marked in green), while the second spin I_k is slightly off the rotor's axis. When the sample is spun with a certain angular frequency ω_R, the internuclear vector r_{jk} circles a cone (marked in blue) and the θ angle becomes a function of time. Regardless of this, the orientation of the effective local field (produced by the spin I_k) with respect to the B_0 remains stable. This feature is also illustrated in *animation 1* available in Supplementary 1.

Knowing the truncated field symmetry it is easy to understand and explain experimental data observed by Pake [11]. In Figure 6(a) two interacting dipolar nuclei (placed in strong B_o field) are illustrated together with an expected NMR spectra recorded for different internuclear vector r_{jk} orientations. Characteristic Pake doublet (also presented in the spectra) is a consequence of spin pair dipolar interaction in the case of powdered sample where r_{jk} orientations are randomly distributed. Red signals in Figure 6(a) represent positions of NMR peaks for the same spin pair measured in the case of single crystall sample. Assumed here local nuclear magnetic field symmetry adequately explains angular dependence of dipolar interaction and predicts nicely vanishing of dipolar splitting at magic angle conditions. It is not surprising because any other effective local magnetic field symmetry would not fit to dipolar Hamiltonian structure which involves 2nd Legendre polynomial determining angular dependence of dipolar coupling strength ($\mathcal{H}_{dd}$ form in spherical coordinates is presented in Supplementary 1).

In order to justify and clarify the truncated field concept, it is worth performing the following thought experiment: imagine a diamond monocrystal enriched with ^{13}C isotope and precisely positioned within NMR probe (equipped with goniometer). The idea is that the experimentator can manually orient the monocrystal with respect to the B_0 field. Figure 7(a) shows the first specific crystall lattice orientation. It is important to note that due to the crystal symmetry, each closest, neighbouring nucleus (μ_j, μ_k, μ_l, μ_m) of μ_i carbon is located onto the magic angle cone surface. In other words, all internuclear vectors are aligned under magic angle conditions with respect to B_0. According to the dipolar Hamiltonian structure, this particular μ_i nucleus experiences solely B_0 field (taking into consideration only interactions with closest neigbours) and somehow it does not sense any local fields produced by its closest neighbours. This remarkable feature can be nicely explained using truncated field symmetry as it is presented in Figure 7(b). The net μ_l local field component along the internuclear vector r_{il} equals zero. Exactly the same holds for other spin pairs presented.

Figure 8(a) shows the second specific crystal lattice orientation. In this particular case none of the nuclear pairs fulfill magic angle conditions. Ilustration 8 8(b) reveals that all the adjacent nuclei are located off-magic angle cone. Consequently, nonzero dipolar coupling is expected.

There are two inequivalent groups of spin pairs: (a) $\mu_i - \mu_m$ and (b) $\mu_i - \mu_j$, $\mu_i - \mu_k$, $\mu_i - \mu_l$. Taking into consideration the dipolar Hamiltonian structure and the truncated field symmetry, it is obvious that r_{im} vector orientation leads to the strongest possible dipolar coupling. It is presented in Figure 9. Three other pairs $\mu_i - \mu_j$, $\mu_i - \mu_k$, $\mu_i - \mu_l$ are equivalent in terms of internuclear vector orientation with respect to the external field B_0. All three vectors r_{ij}, r_{ik}, r_{il} are tilted with respect to B_0 with angle $\theta \sim 70.5^\circ$. According to 2nd Legendre polynomial relation the dipolar coupling in this particular case should be scaled with $D_{il} \sim 0.65$ prefactor (Figure 9). In order to verify if the truncated symmetry fulfills this condition it is possible to (a) magnify the truncated field produced by μ_l until it reaches μ_i position and (b) normalize the truncated field to get $p = 2$ (and automatically $q = 1$). This procedure is illustrated on the right hand side in Figure 9. In order to calculate the angular dependent dipolar coupling prefactor D_{il} we have to find the distance x. For normalized truncated field x is equal exactly 0.65 which is in agreement with the dipolar Hamiltonian structure.

In order to understand the idea of the MAS technique and the process of dipolar coupling averaging, it is worth imagining the internuclear vector evolution under MAS conditions. In

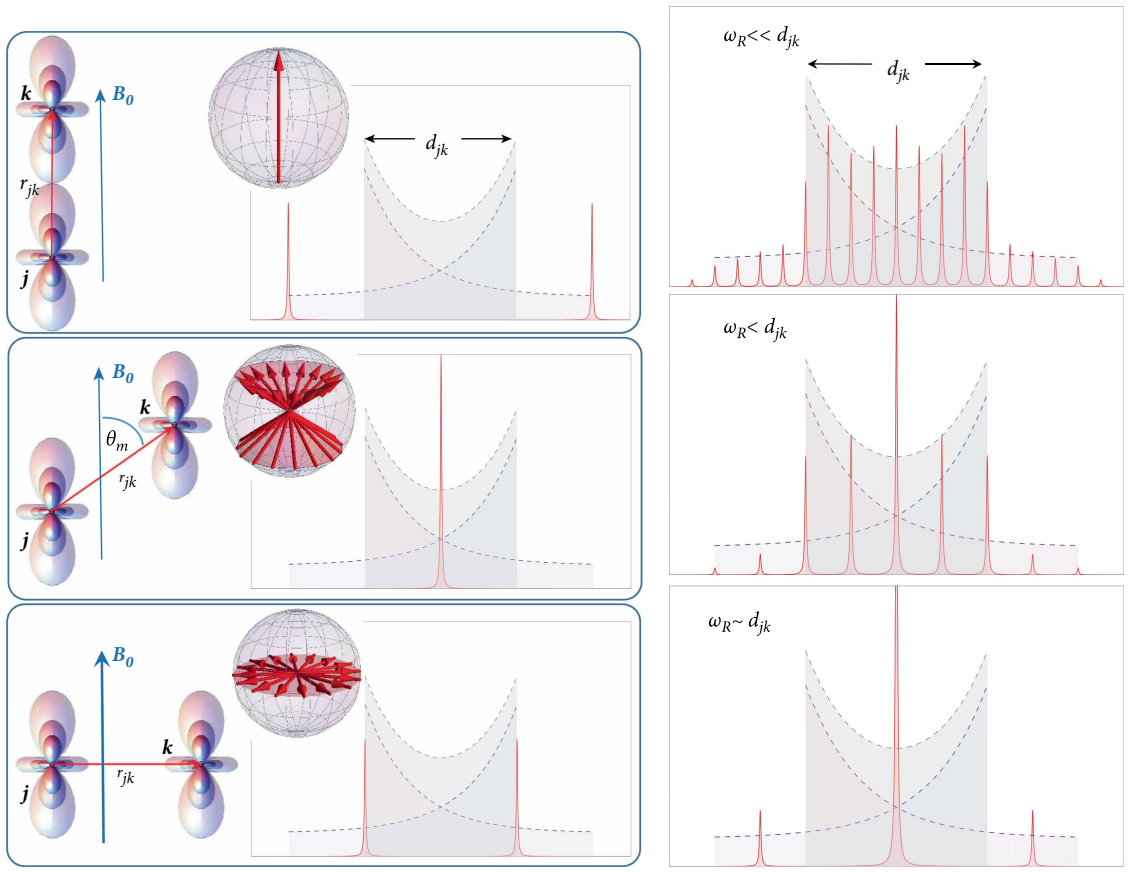

FIGURE 6: (a) Pake doublet (powdered crystall) and dipolar splitting (single crystall) observed for interacting pair of spins with different r_{jk} orientations with respect to B_0. Red vectors in the spheres represent a set of equivalent r_{jk} orientations. (b) effect of MAS on Pake doublet.

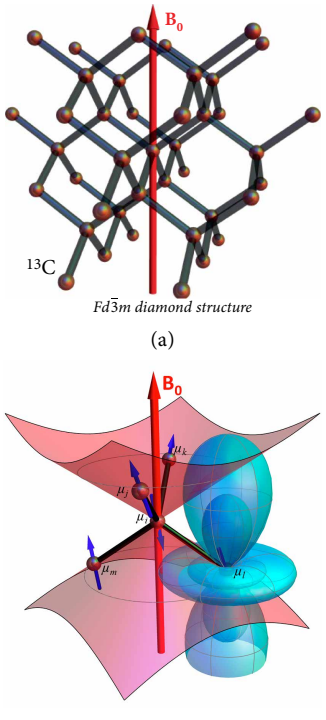

FIGURE 7: (a) Diamond crystal orientation with respect to B_0. (b) Closest neighbours μ_j, μ_k, μ_l, and μ_m located onto the magic angle cone surface.

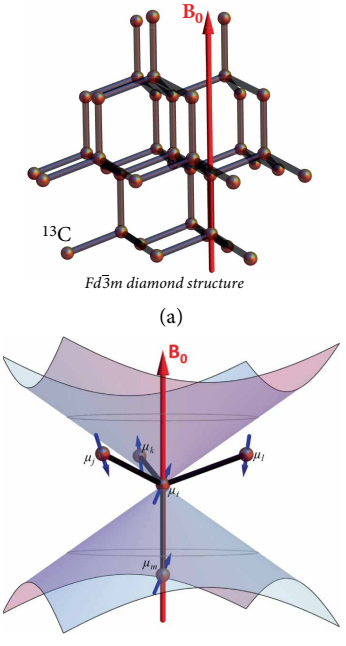

FIGURE 8: (a) Diamond crystal orientation with respect to B_0. (b) Closest neighbours μ_j, μ_k, μ_l, and μ_m located off the magic angle cone surface.

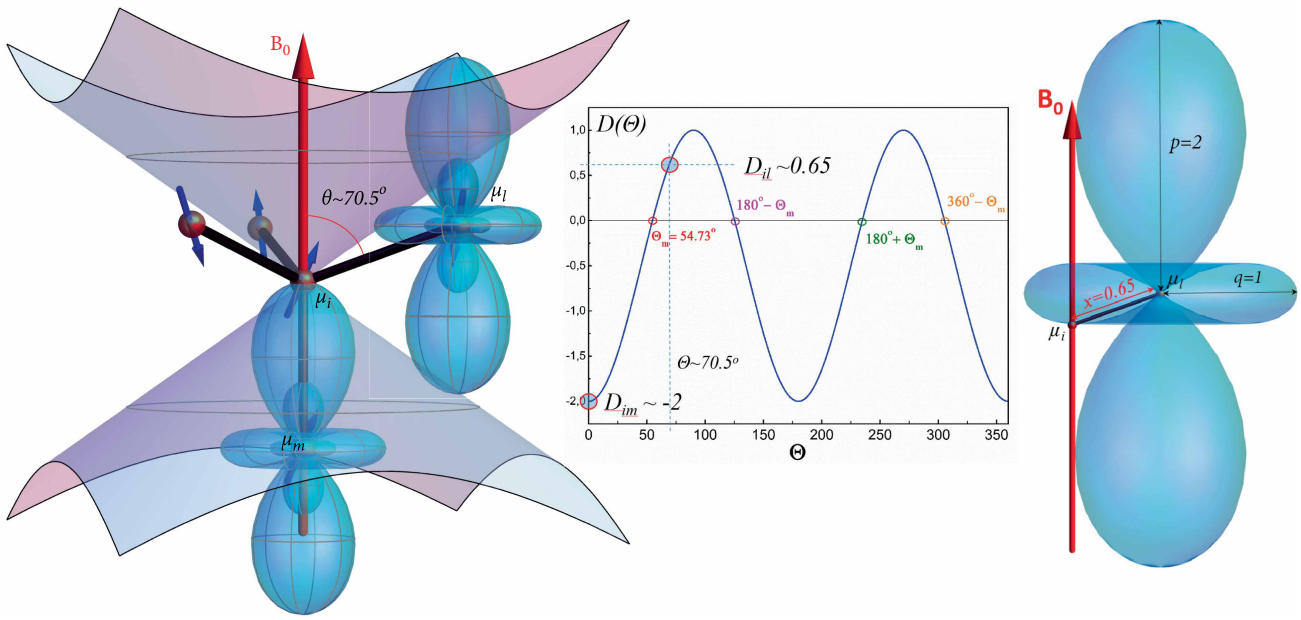

FIGURE 9: The truncated field symmetry correctly explains the angular dependence of the dipolar coupling strength.

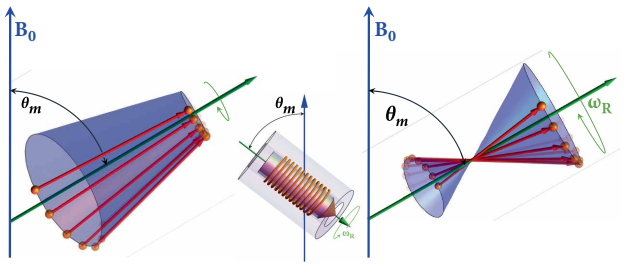

FIGURE 10: Schematically presented evolution of a spin pair under MAS conditions for two different internuclear vector orientations r_{jk} (marked in red) with respect to the rotor's main axis (marked in green).

Figure 10 two examples of randomly oriented r_{jk} (with respect to the main rotor axis) are shown. To illustrate the periodical character of θ angle evolution, let us imagine pair of spins μ_j and μ_k distanced by $r_{jk} = 1$ vector which is oriented 45° with respect to the rotation axis (green arrow) as depicted in Figure 11(b). It is clear that under spinning conditions the r_{jk} vector will slide onto the cone surface with apex angle equal to 90°. This precession-like movement will lead to periodic $\theta(t)$ variation around the magic angle θ_m as illustrated in Figure 11(a). Taking into consideration the dipolar Hamiltonian structure it is easy to calculate the dipolar coupling factor D which is a function of time and θ. The $D(\theta, t)$ evolution is also presented in Figure 11(a). It is worth examining this function in detail because: (a) its evolution proves that the nucleus produces the effective magnetic field (truncated field) having $Y_2^0(\varphi, \theta)$ symmetry, and (b) it shows that the precessing internuclear vector r_{jk} samples this nuclear magnetic field symmetry. Along one rotation period the $D(\theta, t)$ function reveals two maxima and two minima. Both minima are indicated in the Figure 11(a) and correspondingly two characteristic scaling factors $D \sim 0.91$ and $D \sim 1.91$ can be identified. The two maxima exhibit exactly the same scaling which is equal to 1. In order to fully understand this specific evolution let us introduce the truncated field generated by μ_j. As depicted in Figure 11(b) this approach enables us to find directly the two characteristic scaling factors corresponding to both minima. Moreover, it is possible to calculate the scaling factor D for each stage of r_{jk} vector evolution during MAS and prove that the product Dr_{jk} envelopes the $Y_2^0(\varphi, \theta)$ surface as it is depicted in Figure 12. Both Figures 11(c), 11(d), 12(c), and 12(d) illustrate the same analysis performed for $r_{jk} = 1$ vector which is oriented 67° with respect to the rotation axis. It is also worth mentioning that the second nucleus μ_k produces exactly the same truncated magnetic field and its orientation with respect to the external magnetic field is time independent as presented in *animation 1* available via Supplementary 1.

2.2. Chemical Shift Anisotropy. Another interaction which can be effectively averaged out by MAS is chemical shift anisotropy (CSA). This interaction usually manifests on NMR spectra recorded for powdered crystal samples, which gives rise to broadened (usually asymmetrical) signals. CSA is a direct consequence of the electronic environment of the nucleus. In contrast to the dipolar coupling, the source of CSA is not an adjacent nucleus but the electronic environment and its interaction with external magnetic field. Following the general tensorial formula, the CSA Hamiltonian can be described using Equation (8)

$$\mathcal{H}_{CSA} = \gamma h\left(I_j \sigma^{PAS} B_o\right), \tag{8}$$

where σ^{PAS} is the chemical shift tensor which can be described as

$$\sigma^{PAS} = \begin{bmatrix} \sigma_{xx}^{PAS} & 0 & 0 \\ 0 & \sigma_{yy}^{PAS} & 0 \\ 0 & 0 & \sigma_{zz}^{PAS} \end{bmatrix}, \tag{9}$$

where the principal components of the tensor are denoted as σ_{xx}^{PAS}, σ_{yy}^{PAS}, and σ_{yy}^{PAS}. They represent the principal axis system

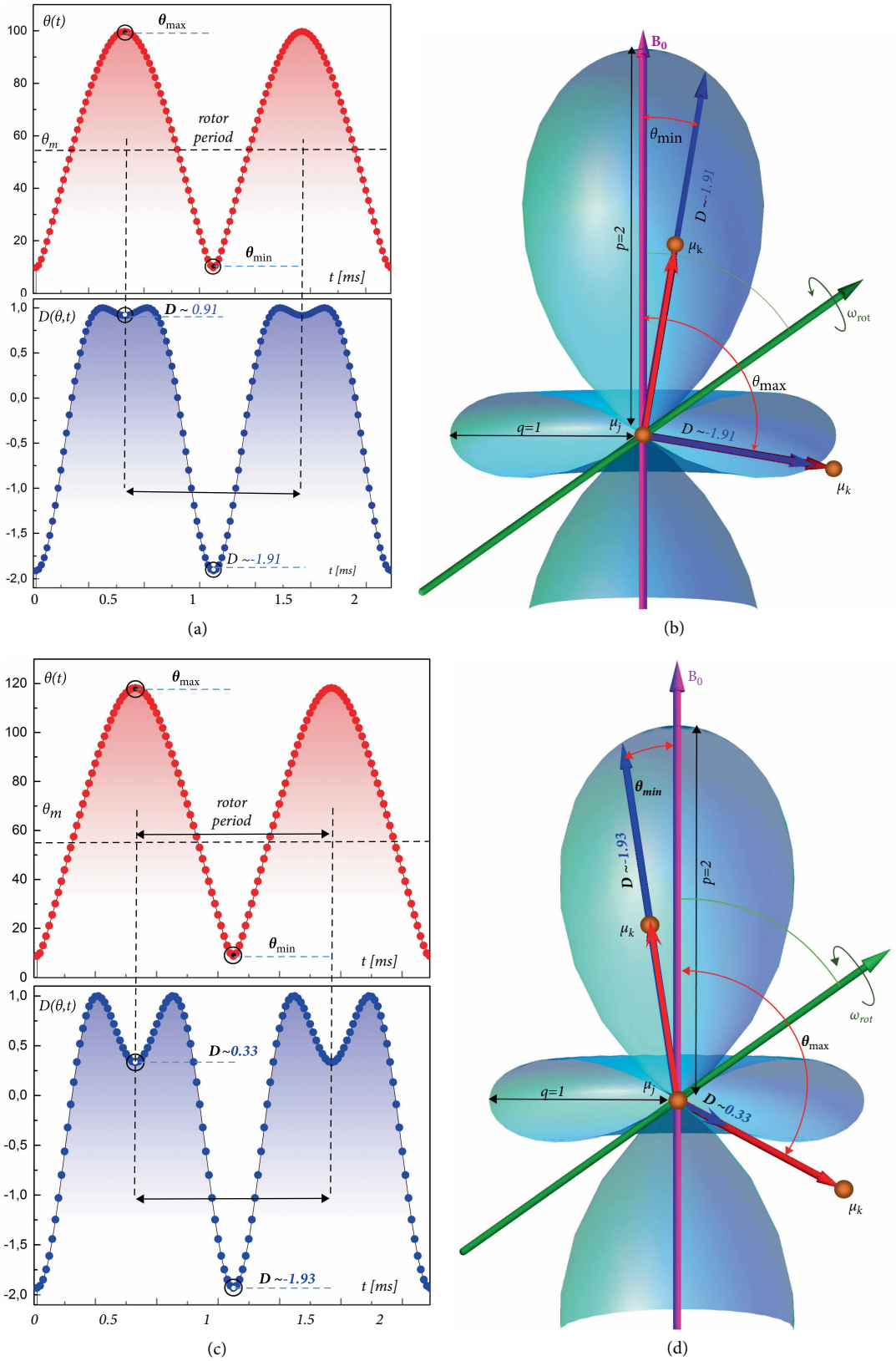

FIGURE 11: (a and c) $\theta(t)$ and $D(\theta, t)$ evolution during MAS, (b and d) two extreme internuclear vector (red) orientations with respect to external magnetic field B_0. Truncated field symmetry of the local nuclear magnetic field generated by μ_j.

(PAS) of the tensor. It is clear from relations equation 6 that effective shielding is directly proportional to the z-component of σ in the laboratory frame determined by the external magnetic field B_0 direction. In other words, it depends on PAS orientation with respect to B_0. This orientational dependence is illustrated in Figure 13, where there are three different

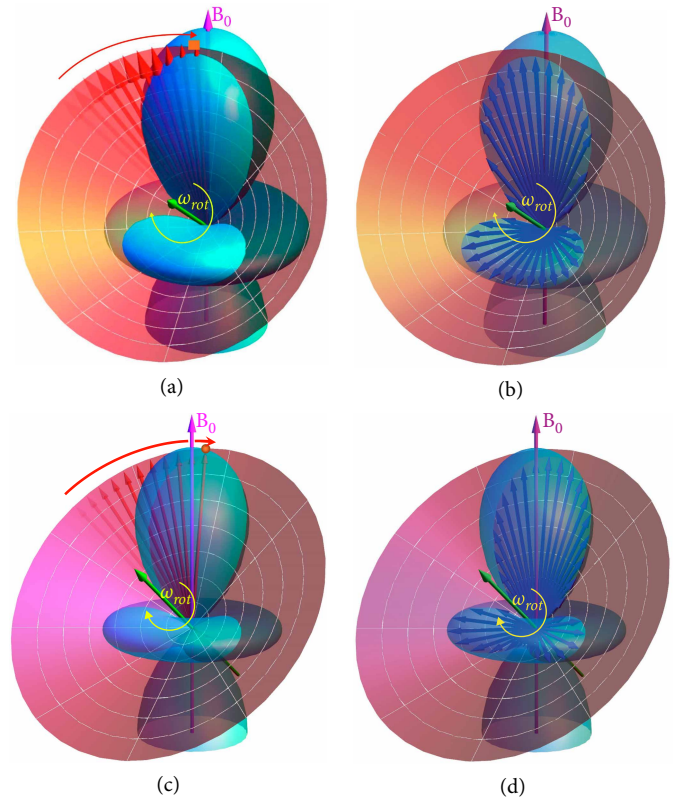

FIGURE 12: (a and c) Illustrate evolution of internuclear vectors (for the case presented in Figures 11(a) and 11(c)) which slide onto different precession cones, (b and d) show that the same internuclear vectors scaled by D precisely envelope the structure of the truncated field.

orientations of hypothetical monocrystals comprising of nuclei exhibiting anisotropic electronic environment (represented by a symmetrical tensor). The component σ_{zz} (marked in red and parallel to B_0) varies as the monocrystal is rotated. Accordingly, an expected NMR signal changes its position on the spectrum. As a result, substantially broadened and asymmetrical, static NMR spectra are often recorded for powdered crystalline samples. Figure 13(b) illustrates that MAS technique allows finding the position of NMR peak characterized for isotropic shielding $\sigma_{iso} = \left(\sigma_{xx}^{PAS} + \sigma_{yy}^{PAS} + \sigma_{zz}^{PAS}\right)/3$. It is easy to distinguish this particular signal from rotational sidebands (marked with stars) due to the fact that its position does not depend on spinning frequency.

In order to understand the generation of rotational sidebands (which are a consequence of periodic modulation of NMR signal due to MAS) it is worth imagining the time evolution of the CS tensor under MAS conditions. In Figure 14 the dynamics of two σ (symmetric and asymmetric, both with arbitrary initial orientations) are illustrated for the spinning experiment. As presented, the principal axis of the tensor σ_{zz}^{PAS} circles a cone around the rotation axis (marked in red) while the σ_{zz} component varies periodically with the angular frequency ω_R. This process is depicted in *animation 2* available in Supplementary 1.

Interestingly, shielding evolution $\sigma_{zz}(t)$ strongly depends on the orientation of PAS with respect to the rotation axis. This inclination can be described by γ angle defined in 15. As indicated, a slightly different initial orientation of the CS tensor leads to significant changes in $\sigma_{zz}(t)$ dependence. This effect is even more pronounced for an asymmetric tensor as presented in 15(b). Evolutions of symmetric and asymmetric CS tensors with different γ positioning are illustrated in *animation 3* and *animation 4* respectively (available in Supplementary 1). It is possible to derive an analytical expression describing the above mentioned evolution and, consequently, calculate the principal CS tensor components directly from the spinning sidebands pattern [12, 13]. It has been shown [13, 14] that NMR signal position is a complex function (10) which depends on both ω_R and γ and can be described in the following way

$$\begin{aligned}\omega = -\omega_0\{&\sigma_{iso} + [A_1\cos(\omega_R t + \alpha) \\ &+B_1\sin(\omega_R t + \alpha)] + [A_2\cos(2\omega_R t + 2\alpha) \\ &+B_2\sin(2\omega_R t + 2\alpha)]\},\end{aligned} \tag{10}$$

where

$$\begin{aligned}A_1 &= \frac{2\sqrt{2}}{3}\sin\gamma\cdot\cos\gamma\left[\cos^2\beta\left(\sigma_{xx}^{PAS} - \sigma_{zz}^{PAS}\right)\right. \\ &\left.+\sin^2\beta\left(\sigma_{yy}^{PAS} - \sigma_{zz}^{PAS}\right)\right], \\ B_1 &= \frac{2\sqrt{2}}{3}\sin\beta\cdot\cos\beta\cdot\sin\gamma\cdot\left(\sigma_{xx}^{PAS} - \sigma_{zz}^{PAS}\right), \\ A_2 &= \frac{1}{3}\left[\left(\cos^2\gamma\cdot\cos^2\beta - \sin^2\beta\right)\left(\sigma_{xx}^{PAS} - \sigma_{zz}^{PAS}\right)\right. \\ &\left.+\left(\cos^2\gamma\cdot\sin^2\beta - \cos^2\beta\right)\left(\sigma_{yy}^{PAS} - \sigma_{zz}^{PAS}\right)\right], \\ B_2 &= -\frac{2}{3}\sin\beta\cdot\cos\beta\cdot\cos\gamma\cdot\left(\sigma_{xx}^{PAS} - \sigma_{yy}^{PAS}\right),\end{aligned} \tag{11}$$

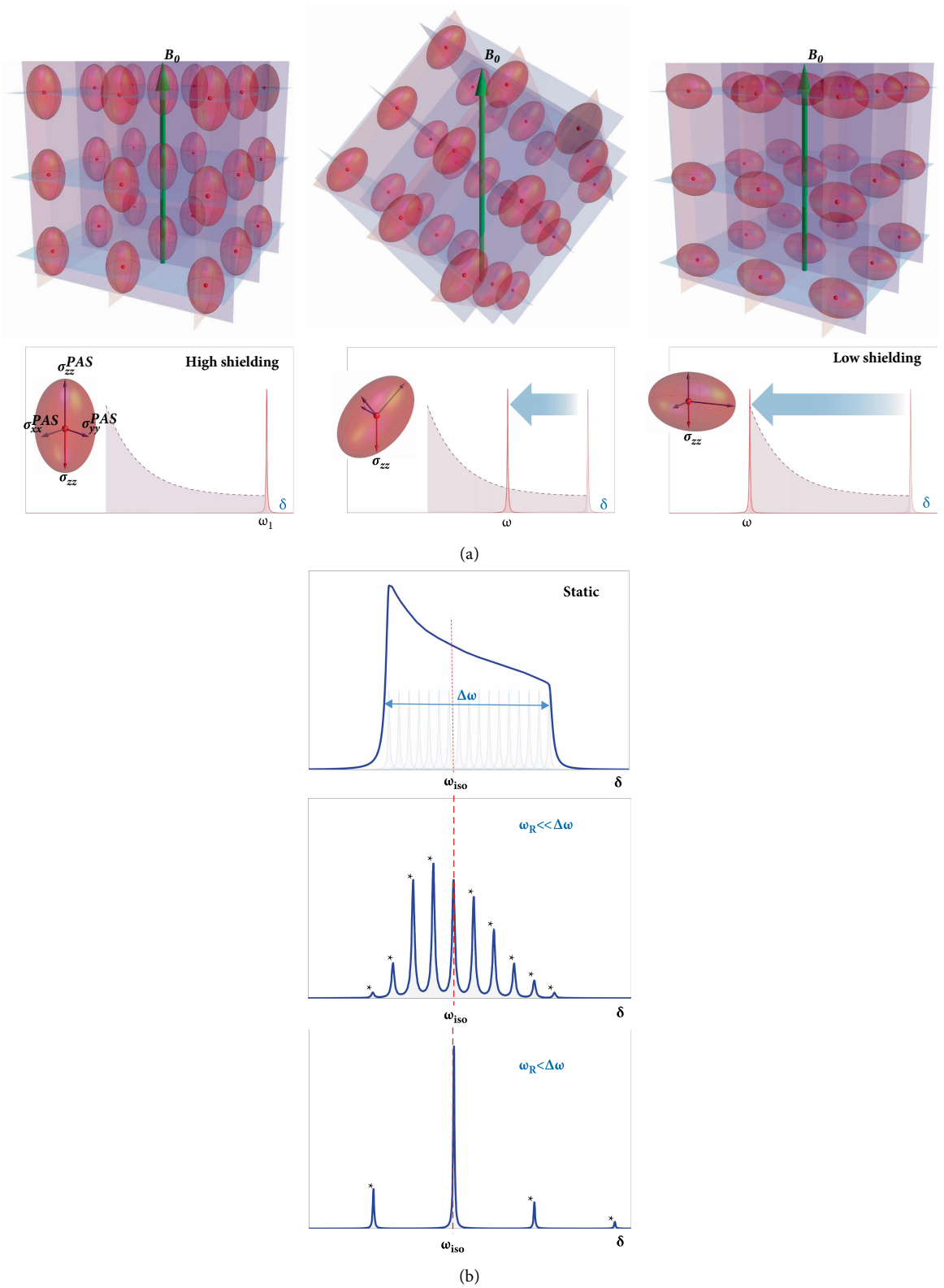

FIGURE 13: (a) Schematically illustrated shielding variation for three different monocrystal orientations with respect to the external magnetic field B_0. (b) Effect of MAS on powdered NMR spectrum.

where α, β, γ are Euler angles describing the orientation of PAS with respect to the rotor axis frame and σ_{iso} represents the isotropic shielding. Detailed derivation of equation 9 and all necessary CS tensor transformations are presented in Supplementary 1. Alternatively, it is also possible to utilize Equation 9 in the case of a static experiment, provided there is a monocrystalline sample available together with an NMR probehead equipped with a goniometer 15. This

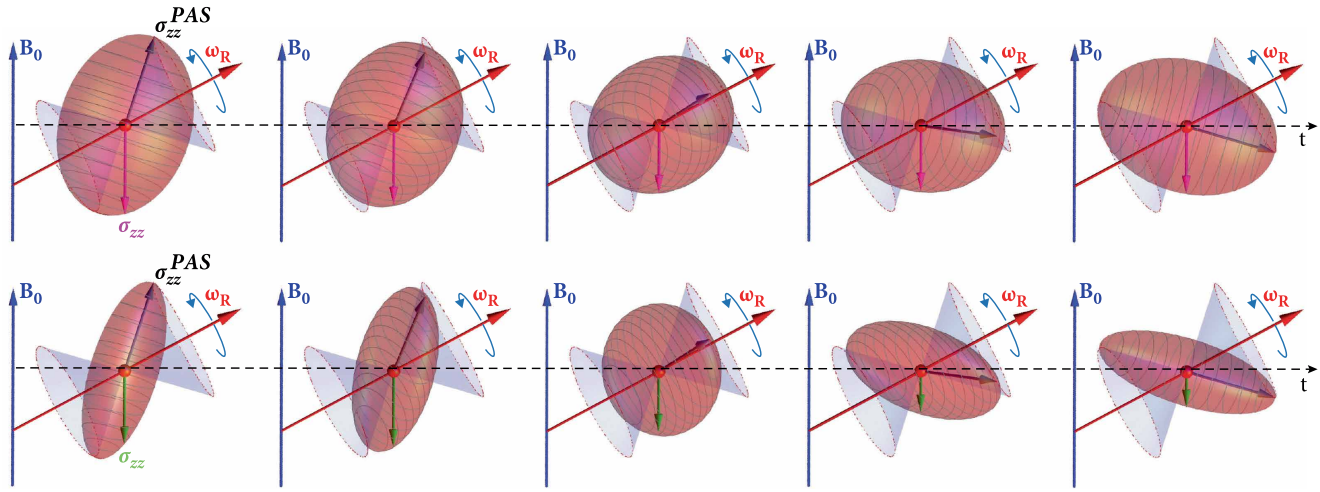

FIGURE 14: The time evolution of CSA tensors (upper symmetric and lower asymmetric) under MAS conditions. Animation available in Supplementary Materials 1.

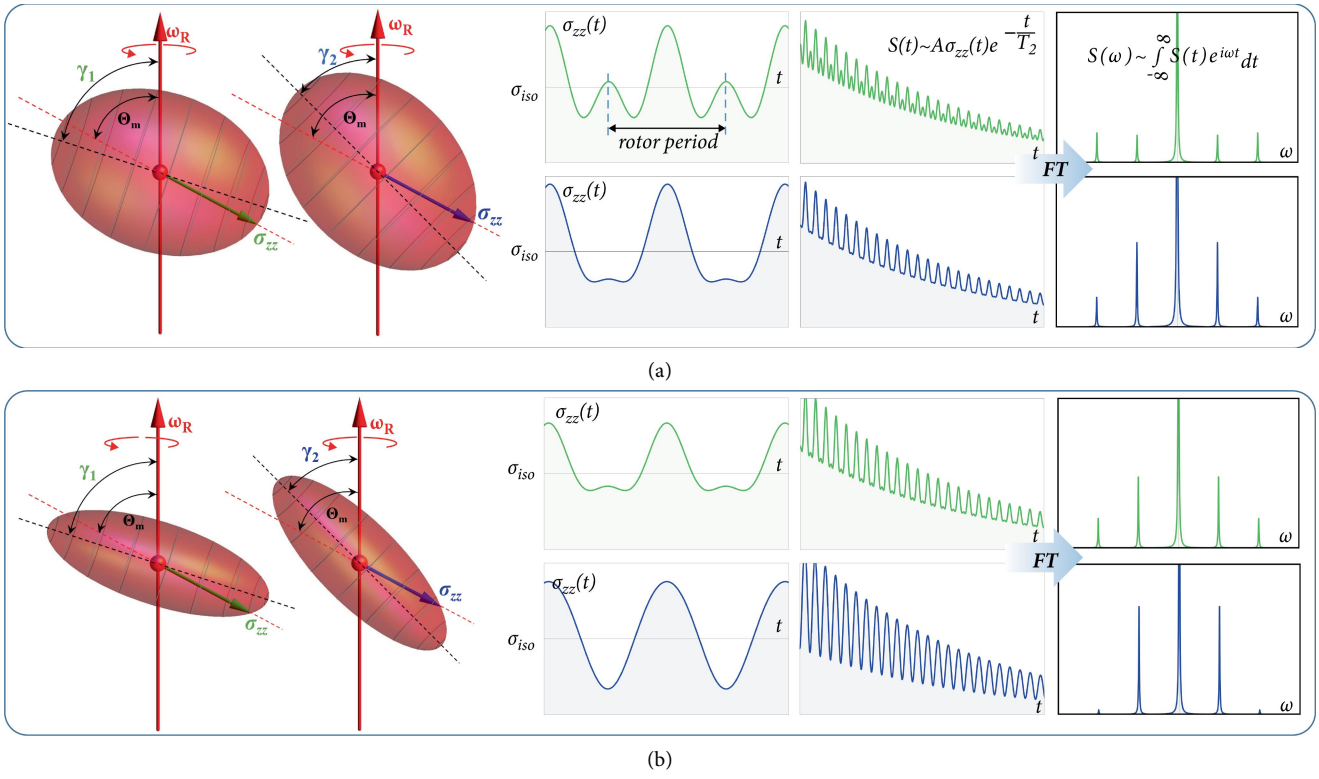

FIGURE 15: $\sigma_{zz}(t)$ time dependencies presented for two different PAS orientations (various γ) with respect to rotor axis frame. (a) Symmetric CSA tensor, (b) asymmetric CSA tensor. On the right hand side simulated FIDs with specified spin-spin relaxation time T_2 are presented together with their Fourier transforms representing expected NMR signals.

allows for sampling chemical shielding for various PAS orientations (manifested as a chemical shift change) and accordingly leads to the determination of principal CS tensor components. As shown in Figure 15 the sideband pattern varies (in terms of amplitudes) for different CS tensor orientations. Presented here NMR spectra are Fourier transforms of simulated FID signals with specified spin-spin relaxation time T_2.

3. Conclusions

Basic concepts regarding spin interactions under MAS conditions can be demanding to comprehend due to an experimentally introduced time evolution of the spin system and its anisotropic properties. In order to thoroughly understand the concept of a MAS experiment it is vital to first describe the structure of coupling tensors and their subsequent

orientational evolution during NMR experiments. The presented work illustrates the fundamental aspects of dipolar interactions and chemical shift anisotropy, and provides transparent graphical examples and animations explaining the anisotropic character of both.

Data Availability

The data used to support the findings of this study are included within the article.

Conflicts of Interest

The authors declare no conflicts of interest.

Supplementary Materials

Supplementary Materials include (i) animations revealing CS tensor evolution under MAS conditions, (ii) dipolar Hamiltonian in spherical polar coordinates, and (iii) CS tensor transformations. (*Supplementary Materials*)

Acknowledgments

The research was supported by the H2020-INFRAIA-2016-2017 under research grant "EUSMI – European infrastructure for spectroscopy, scattering and imaging of soft matter", contract number GA731019, funded under H2020-EU.1.4.1.2.–RIA.

References

[1] E. R. Andrew, A. Bradbury, and R. G. Eades, "Nuclear magnetic resonance spectra from a crystal rotated at high speed," *Nature*, vol. 182, no. 4650, pp. 1659–1659, 1958.

[2] I. J. Lowe, "Free induction decays of rotating solids," *Physical Review Letters*, vol. 2, pp. 285–287, 1959.

[3] J. W. Hennel and J. Klinowski, "Magic-angle spinning: a historical perspective," in *New Techniques in Solid-State NMR*, J. Klinowski, Ed., pp. 1–14, Springer, Berlin, 2005.

[4] Y. Nishiyama, "Fast magic-angle sample spinning solid-state NMR at 60–100 kHz for natural abundance samples," *Solid State Nuclear Magnetic Resonance*, vol. 78, pp. 24–36, 2016.

[5] M. S. Vinding, T. O. Kessler, and T. Vosegaard, "A simple low-cost single-crystal NMR setup," *Journal of Magnetic Resonance*, vol. 269, pp. 120–127, 2016.

[6] Z. Fojud, P. Herzig, O. Żogał et al., "Electric-field-gradient tensor and boron site-resolved ^{11}B NMR in single-crystalline YB_{12}," *Physical Review B*, vol. 75, no. 18, p. 184102, 2007.

[7] F. Blanc, C. Coperet, A. Lesage, and L. Emsley, "High resolution solid state NMR spectroscopy in surface organometallic chemistry: access to molecular understanding of active sites of well-defined heterogeneous catalysts," *Chemical Society Reviews*, vol. 37, no. 3, pp. 518–526, 2008.

[8] S. Ravets, H. Labuhn, D. Barredo, T. Lahaye, and A. Browaeys, "Measurement of the angular dependence of the dipole-dipole interaction between two individual Rydberg atoms at a forster resonance," *Physical Review A*, vol. 92, no. 2, p. 020701, 2015.

[9] B. Laburthe-Tolra, "Quantum dipolar gases in boson or fermion flavour," *Physics*, vol. 5, p. 58, 2012.

[10] R. E. Wasylishen, *Dipolar and Indirect Coupling Tensors in Solids. eMagRes*, John Wiley & Sons, Ltd., Hoboken, NJ, USA, 2007.

[11] G. E. Pake, "Nuclear resonance absorption in hydrated crystals: fine structure of the proton line," *The Journal of Chemical Physics*, vol. 16, no. 4, pp. 327–336, 1948.

[12] Y. S. Avadhut, J. Weber, and J. Schmedt auf der Günne, "Accurate determination of chemical shift tensor orientations of single-crystals by solid-state magic angle spinning NMR," *Journal of Magnetic Resonance*, vol. 282, pp. 89–103, 2017.

[13] M. M. Maricq and J. S. Waugh, "NMR in rotating solids," *The Journal of Chemical Physics*, vol. 70, no. 7, pp. 3300–3316, 1979.

[14] M. J. Duer, "Essential techniques for spin-½ nuclei," in *Solid-state NMR Spectroscopy Principles and Applications*, pp. 73–110, Blackwell Science Ltd, Hoboken, NJ, USA, 2007.

[15] N. Janes, S. Ganapathy, and E. Oldfield, "Carbon-13 chemical shielding tensors in L-threonine," *Journal of Magnetic Resonance (1969)*, vol. 54, no. 1, pp. 111–121, 1983.